ACS APPLIED BIO MATERIALS

www.acsabm.org Article

Assessing Fab-Functionalized Gold Nanoparticles-Mediated Thermal Enhancement during High-Intensity Focused Ultrasound Ablation in a Mouse Tumor Model

Nabin Khanal, Michael A. Marciniak, Marie-Christine Daniel, Liang Zhu, Charles Dumoulin, Keith Stringer, Matthew R. Myers, Pavel Yarmolenko, and Rupak K. Banerjee*

Cite This: ACS Appl. Bio Mater. 2025, 8, 9696−9708 Read Online

ACCESS | Metrics & More | Article Recommendations | Supporting Information

ABSTRACT: High-intensity focused ultrasound (HIFU) stands out as a noninvasive modality that is gaining prominence for the localized treatment of malignant tumors. A mouse tumor model was used to assess the level of thermal enhancement afforded by Fab-functionalized gold nanoparticles (gNPs) during HIFU treatment. Prostate cancer cells (PC3) were used to grow tumors on the right flank of immunodeficient NSG mice. Three levels of gNPs concentrations (0%, 0.019%, and 0.125%) were injected directly into the tumors. HIFU sonication was performed at acoustic power levels of 30W, 40W, and 50W for the duration of 16 s inside a 1.5 T magnetic resonance system. Temperature rise data were recorded for each power level and gNPs concentration during the experiment and analyzed. Tumors were harvested 4 h after the sonication for a histopathology study. A histopathology study was conducted using hematoxylin and eosin (H&E) as well as cleaved caspase 3 (CC3) staining. For an acoustic power of 50W, temperature increases of 16.77 ± 2.33 °C, 19.95 ± 2.98 °C, and 27.78 ± 5.31 °C were recorded for gNPs concentrations of 0%, 0.019%, and 0.125%, respectively. Also, for an acoustic power of 50W, thermal doses of 0.08, 282.87, and 31563.70 min were obtained for gNPs concentrations of 0%, 0.019%, and 0.125%, respectively. Cellular damage around the focus was observed in histopathology studies using H&E staining in HIFU-treated tumors.

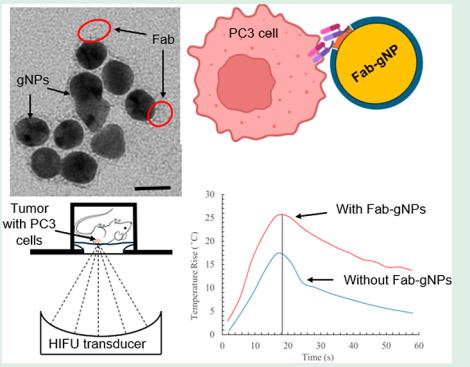

KEYWORDS: *HIFU, Fab-gNPs, gNPs, prostate cancer, tumor ablation, CC3 antibody*

INTRODUCTION

High-intensity focused ultrasound (HIFU) is a noninvasive procedure that has gathered clinical interest for tumor ablation. Treatments involving HIFU find clinical applications[1] in areas such as cancer treatment (including metastatic bone growth and brain tumors), uterine fibroids, thyroid nodules, and neurological disorders (including essential tremor and Parkinson's disease). In cancer treatment, HIFU has gained interest as a novel minimally invasive method for ablating solid tumors in the prostate, breast, kidney, and liver. Its effectiveness in cancer treatment has been demonstrated through in vitro models,[2−5] in vivo models,[6−11] and computational methods.[12−15] The key to HIFU's therapeutic application in treating tumors lies in applying sufficient acoustic power to induce necrosis in the targeted tissue region.[16] However, challenges arise as high acoustic power may inadvertently cause collateral damage to superficial and neighboring tissues, resulting in issues such as skin burns and damage to blood vessels and nerve cells.[17,18] Despite these challenges, HIFU offers distinct advantages in precision and efficacy compared to other ultrasound-based therapies such as low-intensity pulsed ultrasound (LIPUS) and extracorporeal shock wave therapy (ESWT). While LIPUS[19] is useful for stimulating bone healing and tissue regeneration, it lacks energy density to ablate solid tumors or fibrotic tissue. ESWT[20]—primarily used for musculoskeletal disorders—relies on mechanical stress and cavitation but cannot match the focused energy deposition and spatial control that HIFU provides.

To mitigate the collateral damage to normal tissues, external heat absorbers,[21] such as intratumoral (IT) administration of metallic nanoparticles,[22,23] have been employed to reduce power requirements and exposure durations. Effective absorption of the ultrasound wave while using the nanoparticles was observed in a study[24] from our group through three different mechanisms (intrinsic absorption, phonon layer, and viscous drag). The size of the gold nanoparticles (gNPs) used in this study is 17 nm. Intrinsic absorption involves the direct conversion of ultrasound energy into heat by the gNPs

Received: May 8, 2025
Revised: September 29, 2025
Accepted: October 2, 2025
Published: October 13, 2025

https://doi.org/10.1021/acsabm.5c00879
ACS Appl. Bio Mater. 2025, 8, 9696−9708

themselves and is the dominant mechanism for very small particles (up to 11 nm), with its effect remaining constant across sizes. Therefore, the effect of the intrinsic absorption is expected to be moderate. Phonon layer attenuation occurs when thermal waves generated at the gNPs−medium interface form a phonon layer that dissipates energy as heat. This mechanism is dominant at intermediate gNPs sizes (11−1000 nm), peaking when the particle size matches the thermal wavelength. Therefore, the phonon layer effect is expected to be appreciable. Viscous drag attenuation arises from shear waves, causing friction between the gNPs and the surrounding medium, thereby converting mechanical energy into heat. It becomes dominant at large sizes (above 1000 nm). Therefore, the viscous drag effect is expected to be insignificant. Even though the nonfunctionalized gNPs show thermal enhancement during HIFU ablation, they lack the targeting capabilities provided by functionalized gNPs used in the current study.

Past In Vitro and In Vivo Studies. Recently, a few researchers have explored the use of multifunctional nanoparticles[25,26] for enhancing thermal effects and decreasing the power required to achieve a desired level of treatment. A literature review presenting data related to nanoparticle concentration and observed thermal effects compared with baseline concentrations is presented in Table 1. Among these pioneering studies, Ahmad Reza Dibaji et al.[3] from our lab utilized magnetic nanoparticles (mNPs) in tissue-mimicking materials (TMM) to measure the HIFU-induced temperature rise using thermocouples. They observed a peak temperature rise of 1.6 and 2 times compared to baseline concentration (0%) when mNPs concentrations of 1% and 3% were used, respectively, for an acoustic power of 14.5W. However, the mNPs concentrations used were toxic and involved doses considerably above those used in clinical practice.[27] In addition, a study by Beik et al.[28] found a 37.5% increased temperature elevation rate in tumors injected with gNPs (0.25 mg/mL concentration) compared to gNPs-free tumors. Devarakonda et al.[29] from our lab utilized mNPs at clinically acceptable concentration levels of 0%, 0.0047%, and 0.047% in TMM. A peak temperature rise of 1.2 and 1.9 times compared to the baseline concentration (0%) for mNPs concentration of 0.0047% and 0.047%, respectively, was observed, for an acoustic power of 14.5W. Kaczmarek et al.[30] found a more than 100% increase in temperature rise when compared to baseline using 4%(w/w) mNPs in agarose gel. It is important to note that this study utilized significantly higher concentrations with potential for unwanted toxicity. In another study utilizing tissue phantoms, Sadeghi-Goughari et al.[31] observed that both heating and cooling rates using HIFU procedures could be greatly improved by injecting gNPs. Recently, in vivo studies have revealed the efficacy of gNPs in achieving enhanced thermal effects. For instance, in a study by Devarakonda et al.[10] from our lab, the impact of gNPs during HIFU procedures was investigated for 0% and 0.125% (v/v) gNPs concentration on mice. The gNPs were injected subcutaneously into the tumor region through intratumoral injection. The peak temperature rise of 1.7 times compared to the baseline concentration (0%) at an acoustic power of 30W was observed for a concentration of 0.125%. The required concentration of 0.125% was administered via the intratumoral route. A study by Wu et al.[5] found that nanoparticles at volume fractions of 1%−3% could achieve over twice the thermal accumulation efficiency compared to the baseline case.

Table 1. Literature on HIFU Mediated by Nanoparticles

researchers	type of experiment	concentration	results compared to baseline (0%)
Dibaji et al.,[3] 2013	in vitro	1%	1.6 times temperature rise
		3%	2 times temperature rise
Beik et al.,[28] 2016	in vivo	0.25 mg/mL	37.5% increase in temperature elevation rate
Devarakonda et al.,[6] 2017	in vitro	0.0047%	1.2 times temperature rise
		0.047%	1.9 times temperature rise
Kaczmarek et al.,[30] 2018	in vitro	4%	2 times temperature rise
Devarakonda et al.,[10] 2019	in vivo	0.125%	1.7 times temperature rise
Wu et al.,[5] 2025	in vitro	1−3%	2 times thermal accumulation efficiency

Functionalized gNPs. All the studies reported above have utilized nontargeted, unfunctionalized gNPs that lack active tumor-targeting capabilities. There is a possibility of injected nontargeted gNPs getting washed away[32] by the bloodstream, diminishing their presence around the tumor and hindering the intended localized temperature enhancement during HIFU treatment. Hoshyar et al.[33] reported that a rapid mononuclear phagocytic system response results in the clearance of uncoated nanoparticles from the bloodstream within a few hours postinjection. Considering this, this study evaluated the use of gNPs functionalized with antibody fragments (Fab) to ensure that they adhere to and enter the tumor cells after injection. This study is significant because functionalized-gNPs-enhanced HIFU therapy under direct/systemic injection holds a high potential for cancer cell necrosis due to its biocompatibility, absence of significant toxicity, and ability to deliver uniform heating. The outcome of this study presents a method that is accurate, more easily applied than the current state-of-the-art techniques, and easily incorporated into future clinical trials.

Type of Injection. Particles lacking targeting functionality are considered nonfunctionalized gNPs and are typically injected directly to the tumor site via the intratumoral route of administration. In contrast, Fab-functionalized gNPs can be delivered either by a tail vein injection or intratumoral route of administration due to their enhanced targeting capabilities.[34−36] These capabilities can facilitate the effective tumor accumulation of gNPs during systemic administration. Ouyang et al.[37] demonstrated that over 15% of functionalized nanoparticles reach the tumor site when administered via the tail vein injection, provided the number of injected nanoparticles exceeds 1 trillion (a condition met in this study). In a previous study from our lab,[10] a 0.125% concentration (maximum) of nonfunctionalized gNPs was used through the intratumoral route of administration. The same higher concentration (0.125%) of Fab-functionalized gNPs was also directly injected at the tumor site in the current study. Further, a medium concentration of 0.019% of Fab-functionalized gNPs—equivalent to 15% accumulation at the tumor site expected[37] from a tail vein injection of 0.125% concentration—was directly injected at the tumor site. Experiments were conducted at three gNPs concentration levels: 0% (control), 0.019% (15% of 0.125%; equivalent of a tail vein injection), and 0.125% (maximum concentration with an

https://doi.org/10.1021/acsabm.5c00879
ACS Appl. Bio Mater. 2025, 8, 9696−9708

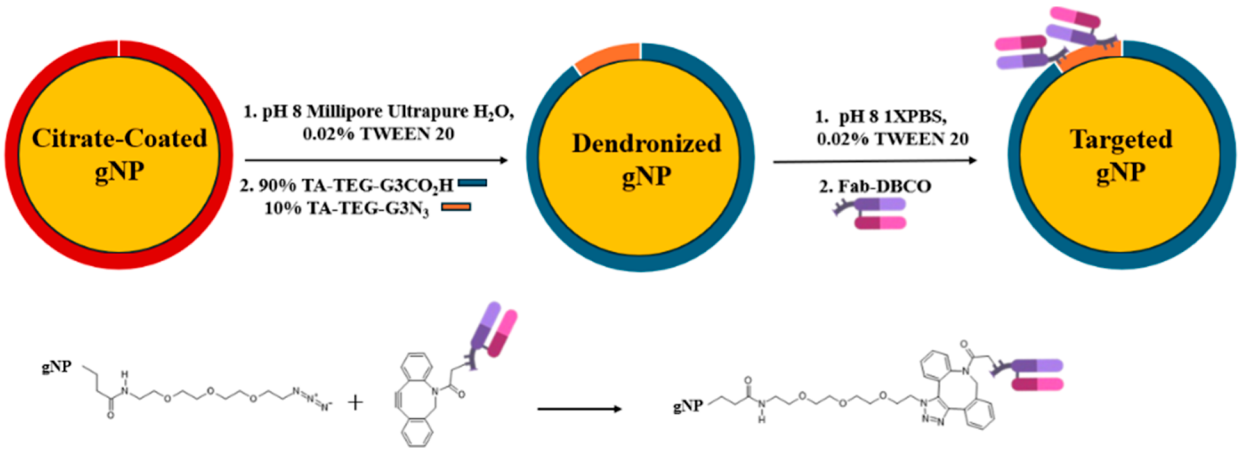

Figure 1. Schematic representation of functionalization of dendronized gNPs with cancer-specific targeting antibody fragment, Fab, starting from citrate-coated gNPs.

intratumoral route of administration); all injected via intratumoral route of administration.

To minimize the potential for gNPs washout during administration, the current study incorporates gNPs that were functionalized with a 5T4 antibody fragment that is specific in targeting tumors. The effect of varying concentrations of Fab-functionalized gNPs on temperature rise and thermal dose induced by HIFU was assessed using an in-house developed mouse model.[38,39] Tumors were grown on the right flank of the mice. All three concentration levels are considered clinically nontoxic.

To the extent we are aware, this acoustic-thermal-functionalized-gNPs research is novel, as it represents the first use of Fab-gNPs-targeted PC3 tissue heating under reduced transducer power in the field of HIFU thermal ablation. The utilization of Fab-functionalized gNPs can offer precisely targeted HIFU sonication of tumors without collateral damage to normal tissues, thereby advancing the field of cancer treatments. Fab-functionalized gNPs are referred to as gNPs in the rest of the manuscript.

METHODS

In this section, the methodology for the development of a mouse tumor model is first introduced. Subsequently, the method of preparation of the gNPs construct is reported. The experimental setup, consisting of a magnetic resonance (MR) HIFU (MR-HIFU) system, is then discussed. Next, the protocols for both MR imaging and thermometry are presented, followed by the experimental procedure. Further, the methodology for the calculation of thermal dose and sonication time is detailed. Lastly, the methodology for the histopathology using hematoxylin and eosin (H&E) and cleaved caspase antibody (cleaved caspase 3 (CC3)) is discussed.

Cell Line and Tumor Development. NOD/SCID GammaC$^{-/-}$ commonly known as, NSG mice[40,41] were purchased from The Jackson Laboratory (Bar Harbor, ME) and maintained by in-house breeding at Cincinnati Children's Hospital and Medical Center (CCHMC, Cincinnati, OH). All animal studies were approved by the Institutional Animal Care and Use Committee (IACUC2021-0042) at CCHMC. To establish the cell line-derived xenograft model, 6 to 8 week-old male mice with a body weight around 30 g were engrafted subcutaneously with 1×10^7 PC3 cells into the right flank. Mice were group-housed under pathogen-free, temperature, and humidity-controlled environmental conditions (21 ± 1.5 °C temperature, 55 ± 10% humidity, and a 12 h light−dark cycle). The tumor growth was monitored for 4−6 weeks. The size of the tumor was measured regularly, 2−3 days per week. Once the tumor was roughly above 10 mm in both the transverse and longitudinal directions, it was deemed suitable for treatment. This was done to ensure that the treatment can be performed in at least two zones of a particular tumor. The tumor volume was 0.2−0.4 mL. Further details about cell culture and mouse model development can be found in our previous works.[38,39]

gNPs Construct Preparation. First, gNP-CO_2H/N_3 dendronized nanoparticles were prepared following several steps reported by Dockery and Daniel[42] (Figure 1). The syntheses of dendrons-coating gNPs are described in the literature.[43] Then, three similar batches of the Fab-functionalized gNPs constructs were obtained through click-chemistry between gNP-CO_2H/N_3 and DBCO-derived Fab (Figure 1). Preparation of all batches followed the same steps with minor differences in concentrations of gNPs. For example, to prepare batch 1, a solution of gNP-CO_2H/N_3 (81 mL, 1.61×10^{13} gNPs/mL) in filtered, pH8 1X PBS (Phosphate-Buffer Saline) was stirred at room temperature in a freshly cleaned 250 mL round-bottom flask. A quantity of 501 μg of Fab-DBCO (taken from 1 mg/mL stock, to provide ∼10 Fab/gNP) was added to this stirring solution. The reagents were stirred for 1 h at room temperature. After 1 h, the reaction was stopped. The solution was centrifuged (45kg, 2 h, 4 °C) and resuspended in 40 mL filtered pH8 1X PBS. This was followed by another centrifugation (45kg, 2 h, 4 °C) with resuspension in 6 mL filtered pH8 1X PBS. Subsequently, a final centrifugation step was carried out (21kg, 1 h, 4 °C), followed by resuspension of gNPs pallets in a total of 2 mL filtered, pH8 1X PBS (final concentration: 0.62×10^{15} gNPs/mL). The carrier fluid for the injection of gNPs was PBS. The resulting concentrated solution was characterized by using DLS and UV−vis spectroscopy. The Z-average of the particle hydrodynamic diameter was 27.49 nm, and the maximum absorption wavelength was 525 nm. Additional details on the synthesis and characterization of Fab-functionalized gNPs are provided as Supporting Information I.

Physiologically relevant concentrations (0%, 0.019%, and 0.125%) of synthesized gNPs were injected directly into the tumor 24 h before the HIFU treatment. Mice were put in an incubator at 40° C for 1 h before gNPs injection to reduce interstitial fluid pressure in the tumor, as suggested by a previous study.[44] Gu et al.[45] demonstrated that gNPs accumulation in PC3 tumors reached a representative level 24 h postintravenous (IV) administration, consistent with findings from other studies. For example, Li et al.[46] and Yu et al.[47] have reported the presence of NPs up to 80−120 h postinjection, indicating that complete clearance of NPs within 24 h is unlikely. Additionally, published data (Hoshyar et al.[33]) indicate that similar NPs exhibit blood clearance half-lives ranging from one to several hours while supporting the assumption that a 24 h interval allows for sufficient tumor accumulation without significant clearance. Therefore, HIFU ablation treatment was scheduled 24 h postinjection based on this established pharmacokinetic profile. Additionally, transmission electron microscopy (TEM) imaging was conducted using tumor

https://doi.org/10.1021/acsabm.5c00879
ACS Appl. Bio Mater. 2025, 8, 9696−9708

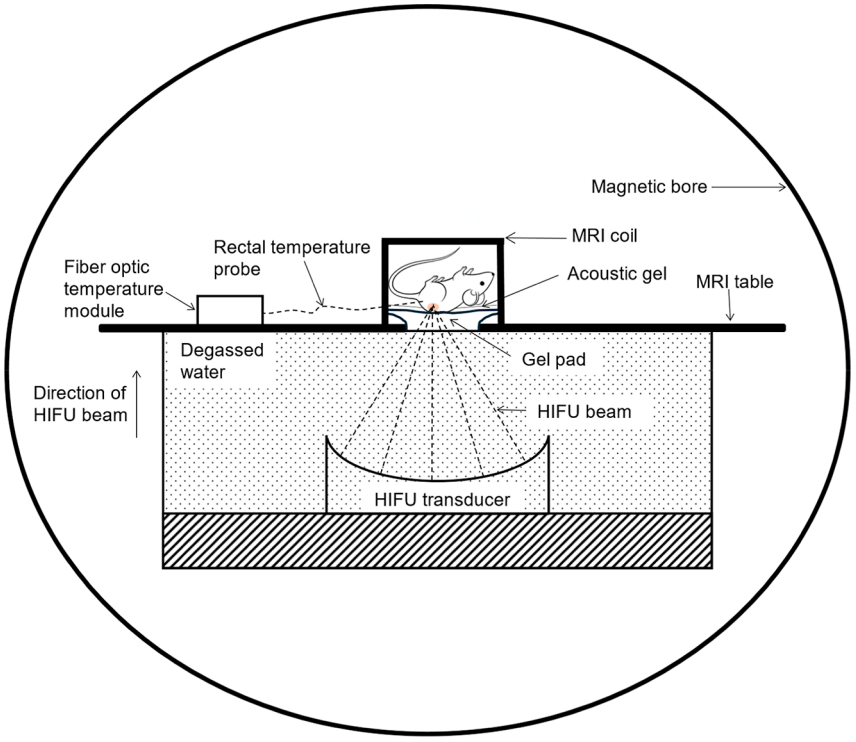

Figure 2. Experimental setup of a mouse under the MR-HIFU system. A MR coil is used to increase the resolution of the MR imaging. A rectal probe is used to monitor body temperature. Acoustic gel is placed to avoid cavitation and bubbles. The beam focus is placed inside the mouse tumor using the integrated MR-HIFU system.

sections of mice from IV and intratumoral (IT) injection. TEM imaging for sections obtained for both IV and IT injections also supported the assumption that a 24 h interval allows for sufficient accumulation of gNPs around the tumor.

The gNPs are assumed to be in a spherical shape and uniformly distributed in the solution used for administration. The volume of the engrafted tumors may vary somewhat among different mice. Therefore, the average tumor volume across all mice was used for calculating the number of gNPs injected, thereby minimizing the statistical variability. The volume of a single gNP of 17 nm diameter is 2.57×10^{-18} cm^3 and 0.125%(v/v) of 1 mL is 0.00125 cm^3. Dividing 0.00125 by 2.57×10^{-18} results in 4.86×10^{14} gNPs. Hence, 4.86×10^{14} gNPs per mL of tumor volume were injected. The tumor volume was 0.2−0.4 mL. For a tumor of 0.2 mL volume, 9.72×10^{13} gNPs (greater than 1 trillion gNPs) were injected. A similar calculation was performed for 0.019%. For the 0.019% case, 1.45×10^{13} gNPs (also greater than 1 trillion gNPs) were injected for a tumor of 0.2 mL in volume. The carrier fluid for gNPs was PBS. The gNPs solution was injected slowly, and the infusion rate was less than 5 μL/s. The solution containing gNPs had a distinct dark red/purple color, such that it can be visible around the tumor after the injection. The mathematical steps for calculating the number of gNPs injected are detailed in Supporting Information II.

MR-HIFU Setup. A clinical MR-HIFU system (Sonalleve V2, Philips Medical Systems, Vantaa, Finland), integrated into a 1.5 T whole body scanner (Philips Ingenia, Healthcare, Best, Netherlands), was used for the scanning of the mouse tumors (Figure 2). The MR-HIFU system contains a 256-element phased array HIFU transducer that can be used to focus energy on small volumes within the tumor. The diameter of the array transducer and the operating frequency are 140 mm and 1.2 MHz, respectively. The focal spot of the HIFU beam was ∼2 mm in the radial direction. Further details about the MR-HIFU system can be found in Devarakonda et al.[10]

Experimental Procedure. On the day of the experiments, the mice were subjected to chemical hair removal (Nair, Ewing, NJ) around the tumor region. Mice were then subjected to intraperitoneal injections with 100 mg/kg of ketamine (Ketaset/Zoetis, Parsippany, NJ) and 10 mg/kg of xylazine (Anased/Akron, Lake Forest, IL) for anesthesia. Two mice were placed on the HIFU transducer for treatment. They were covered with acoustic gel to avoid the formation of bubbles and cavitation. MR images were taken before and after the treatment. The treatments were done by first locating the tumor with test sonication and then applying the assigned power with therapy sonication for 16 s[6,10] The temperature rise was observed and recorded for analysis using MR Thermometry. The mice were kept for 4 h after treatment under analgesia and then euthanized using carbon dioxide, followed by the secondary physical method of cervical dislocation (approved by IACUC2021-0042). The mice were assigned randomly to different groups to avoid the effect of the tumor shape and size on ablation.

A statistical power analysis was conducted to determine the appropriate sample size based on prior data reported by Devarakonda et al.[10] Considering concentration being the primary experimental predictor of the temperature increase with three levels (0%, 0.0625%, and 0.125%), a one-way ANOVA method was employed to assess the statistical power. The effect size was estimated from the observed temperature rise data.[10]

The effect size in one-way ANOVA is calculated using the following formula:

$$f = \sqrt{\frac{\frac{1}{3}(\mu_i - \bar{\mu})^2}{\sigma}} \quad (1)$$

where f is the effect size, μ_i is the group means of temperature rise, i = 1, 2, 3 are three concentration levels, $\bar{\mu}$ is the overall mean of temperature rise, and σ is the estimate of population common standard deviation. Using the temperature rise data observed in Devarakonda et al.,[10] μ_1 was 19.6, μ_2 was 25.8, μ_3 was 34.4, $\bar{\mu}$ was 25.9, and σ was 8.9. By substituting these values in eq 1, an effect size of 0.58 was calculated, which resulted in an observed statistical power of 71% (less than standard of 80%).

The current study aimed to achieve a statistical power $(1 - \beta)$ of 80% with a significance level (α) of 0.05. Power analysis indicated that for an expected effect size of 0.58, a minimum of 11 subjects per

https://doi.org/10.1021/acsabm.5c00879
ACS Appl. Bio Mater. 2025, 8, 9696−9708

group would be required to meet this criterion. The available budget supported a sample size of 12 subjects per group, which allowed the detection of an improved effect size of 0.55 with 80% power. The experiment included three concentration levels (0%, 0.019%, and 0.125%), with 12 subjects assigned to each level, resulting in a total of 36 samples (12 × 3). Since each concentration involves three power levels, four mice (n = 4) per concentration per power were selected. R-markdown (RStudio Team (2022), Boston, MA) software was used for analysis.

HIFU Sonication. After the mice were aligned inside the imaging coil, MR images using T_1-weighted and T_2-weighted sequences were obtained in both sagittal and coronal planes. Further details about the MR imaging can be found in previous publications.[10] Subsequently, after determination of the tumor location, the ultrasound beam was focused inside the tumor. The optimized temporal resolution of the temperature measurements was 3 s. Three acoustic powers of 30, 40, and 50W were used for the HIFU sonication. All power values provided were derived from the radiation force balance measurements.

Temperature Measurements. The initial temperature of each animal was obtained from an MR-compatible rectal probe (SA Instruments Inc., Stony Brook, NY, USA). During the sonication and cooling periods of 16 and 40 s, respectively, MR thermometry was used to acquire temperature data. Temperatures were measured at 6 points during the heating phase and 11 points during the cooling phase. Peak pixel temperature at the end of the sonication was compared between different concentrations of injected gNPs.

Absorbed Energy. In addition to the temperature rise , absorbed ultrasound energy (W/m^3) due to the presence of gNPs was also calculated. This was computed from the initial (first two time-points) temperature values calculated from the MR thermometry. In the initial duration, heat conduction can be neglected. Thus, in this scenario, temperature rise is related to the absorbed energy Q by

$$Q = \rho_0 c_p \frac{\partial T}{\partial t}\Big|_{t=0} \tag{2}$$

where ρ_0 is the density of the tissue, c_p is the specific heat capacity of the tissue, T is the temperature, and t is the time. The initial time derivative was determined by fitting a line to the first two data points on the time axis. The ratio of the absorbed ultrasound energy with and without gNPs was computed for the different powers used during experiments.

Thermal Dose. The thermal dose corresponding to a temperature $T(t)$ was calculated using the method developed by Sapareto and Dewey.[48] The thermal dose parameter is obtained by

$$t_{43}(x, y, z) = \int_{t=0}^{t=t_{final}} R^{43-T(t)} dt \tag{3}$$

where t_{43} is the thermal dose at the reference temperature of 43 °C, t_{final} is the treatment (sonication + cooldown) time, $T(t)$ is the temperature (in °C) as a function of time obtained experimentally at the focal location, and

$$R = \begin{cases} 0.5 & \text{if} T(t) \geq 43^\circ C \\ 0.25 & \text{otherwise} \end{cases} \tag{4}$$

For all thermal-dose calculations, a trapezoidal scheme was used to perform the integration with a time increment of dt = 0.5 s.

Number of Heating Sessions. A tissue is considered necrosed when the thermal dose (t_{43}) value is above 240 equiv minutes. The number of heating sessions required to reach a thermal dose of 240 min is obtained from

$$\text{Number of heating sessions} = \frac{240}{t_{43}} \tag{5}$$

where t_{43} is the thermal dose and is obtained from eq 3.

Tissue Processing and Staining for Histopathology. Four hours after HIFU application, mice were euthanized using carbon dioxide, followed by the secondary physical method of cervical dislocation (approved by IACUC2021-0042). Tumors were immediately harvested, photographed, and fixed in neutral buffered formalin prior to paraffin embedding. Four consecutive sections with a thickness of 4 μm (16 μm in total) were cut at multiple sampling sites, the sites located 330 μm apart from one another. For histopathological analysis, the first tumor section was stained with H&E, while the second section was stained with CC3 antibody using diaminobenzidine as a chromogen for immunohistochemistry. Quantitative analysis of CC3 antibody-stained tissue sections was performed using the positive pixel count software Leica (Leica Microsystems Inc., Buffalo Grove, IL) on scanned images. The apoptotic index was calculated as the ratio (Nsr) of the number of strongly positive cells (Nsp) to the total number of positively stained cells (Ntp). A higher Nsr value indicates a greater proportion of apoptotic cells. For each tissue section, rectangular regions of identical dimensions were defined using the software to systematically capture the entire section. The three regions with the highest Nsr values were selected, and their average was used for comparative analysis across samples.

RESULTS

The thermal maps shown in this section are obtained from MR thermometry. Temporal variations of maximum pixel temperature increase obtained from thermal maps are plotted. The maximum temperature rise is observed at the end (t = 16 s) of the sonication. Maximum temperature increases are compared between different gNPs concentrations. The temperature data reported in this section represents the average values measured for four mice (n = 4). The average thermal doses are calculated using eq 2. Additionally, sonication time is calculated to achieve the 240 equiv minutes of required thermal dose to damage the tumor. Furthermore, the result of the histopathology study of the harvested tissues following HIFU sonication is reported in this section.

MR-HIFU-Induced Temperature Maps. Figure 3 shows the plane of maximum pixel temperature obtained during MR thermometry for the concentrations of 0%, 0.019%, and 0.125% gNPs (shown in columns) and for the powers of 30, 40, and 50W (shown in rows). The color bar represents

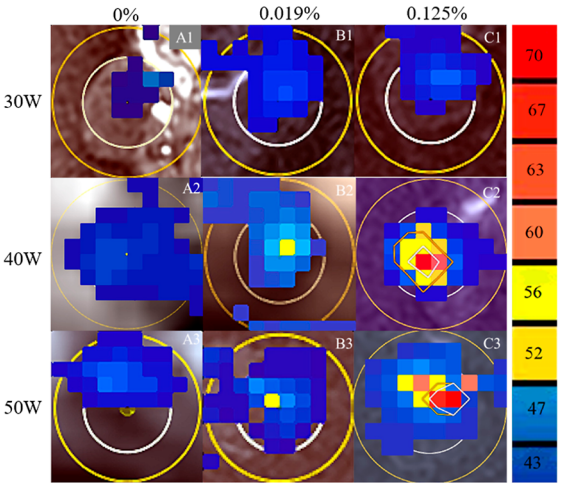

Figure 3. Representative temperature maps inside the mouse tumors at maximum temperature with 0%, 0.019%, and 0.125% gNPs concentration for the acoustic powers of 30W, 40W, and 50W. The thermal maps are obtained at the end of the sonication period (16s). (A1, A2, A3) Thermal maps for 0% gNPs concentration. (B1, B2, B3) Thermal maps for 0.019% gNPs concentration. (C1, C2, C3) Thermal maps for 0.125% gNPs concentration.

https://doi.org/10.1021/acsabm.5c00879
ACS Appl. Bio Mater. 2025, 8, 9696−9708

temperatures in° C. The gradient of blue, yellow, orange, and red colors indicate increasing temperature values, where blue represents the lowest and red represents the highest values. Importantly, an increase in temperature is observed with increasing gNPs concentration (from top to bottom). An increasing trend in temperature (red pixels) is also observed with increasing acoustic powers (from left to right). Quantified temperature profiles of peak pixel temperature are discussed below.

Peak Temperature Profiles. Figure 4 shows the maximum pixel temperature within the tumor as a function of time. The initial 16 s (x-axis) represents the heating (sonication) period, whereas the time beyond 16 s represents the cooldown period. In Figure 4A−C, the temperature rise at the end of the heating period (16 s) is the maximum temperature rise. For the 30W power level, the temperature rise at the end of sonication is 8.5, 11.3, and 11.4 °C for gNPs concentrations of 0%, 0.019%, and 0.125%, respectively. For the 40W power level, the temperature rise at the end of sonication is 14.8, 17.2, and 19.7 °C for gNPs concentration of 0%, 0.019%, and 0.125%, respectively. Similarly, for the 50W power level, the temperature rise at the end of sonication is 16.8, 19.9, and 27.8 °C for gNPs concentrations of 0%, 0.019%, and 0.125%, respectively. Therefore, the temperature increase for the 30W power level at the end of sonication is 33% and 34% higher for 0.019% and 0.125% concentrations, respectively, as compared to the baseline case. The temperature rise for the 40W power level at the end of sonication is 16% and 33% higher for 0.019% and 0.125% concentrations, respectively, as compared to baseline. On a similar note, the temperature increase for the 50W power level, at the end of sonication, is 18% and 65% higher for 0.019% and 0.125% concentrations, respectively, as compared to the baseline case.

For the 30W power level, the temperature rise at the end of sonication is 2.8 and 2.9 °Chigher for 0.019% and 0.125% gNPs concentrations, respectively, in relation to the baseline case. For the 40W power level, the temperature rise at the end of sonication is 2.4 and 4.9 °C higher for 0.019% and 0.125% gNPs concentration, respectively, in relation to the baseline case. For the 50W power level, the temperature rise at the end of sonication is 3.1 and 11 °C higher for 0.019% and 0.125% gNPs concentration, respectively, in relation to the baseline case. Overall, the difference in temperature increase relative to 0% (baseline) concentration was observed to increase with increasing gNPs concentrations and power levels.

Group Mean of Temperature Rise. Table 2 shows the p-value obtained from two-way ANOVA analysis. It is evident that the concentration is nearly a significant factor with p = 0.058 (Table 2). Similarly, power is also a significant factor with $p < 0.05$ (p = 0.001, Table 2). However, the interaction between concentration and power is not significant with $p > 0.05$ (p = 0.733, Table 2). Figure 5A,B shows the group means of temperatures rising with p-values obtained by multiple comparison of means on concentrations and powers using Tukey contrasts. It shows that there is a statistically significant difference in mean temperature rise between 0% and 0.125% with $p < 0.05$ (p = 0.048, Figure 5A) and a statistically insignificant difference between 0% and 0.019% and 0.019% and 0.125% concentrations with $p > 0.05$ (p = 0.385 and p = 0.447, Figure 5A). Further, it shows that there is a statistically significant difference in mean temperature rise between 30W and 40W, and 30W and 50W, with both $p < 0.05$ (p = 0.025 and p = 0.001, Figure 5B) and a statistically insignificant difference between 40W and 50W powers with $p > 0.05$ (p = 0.282, Figure 5B).

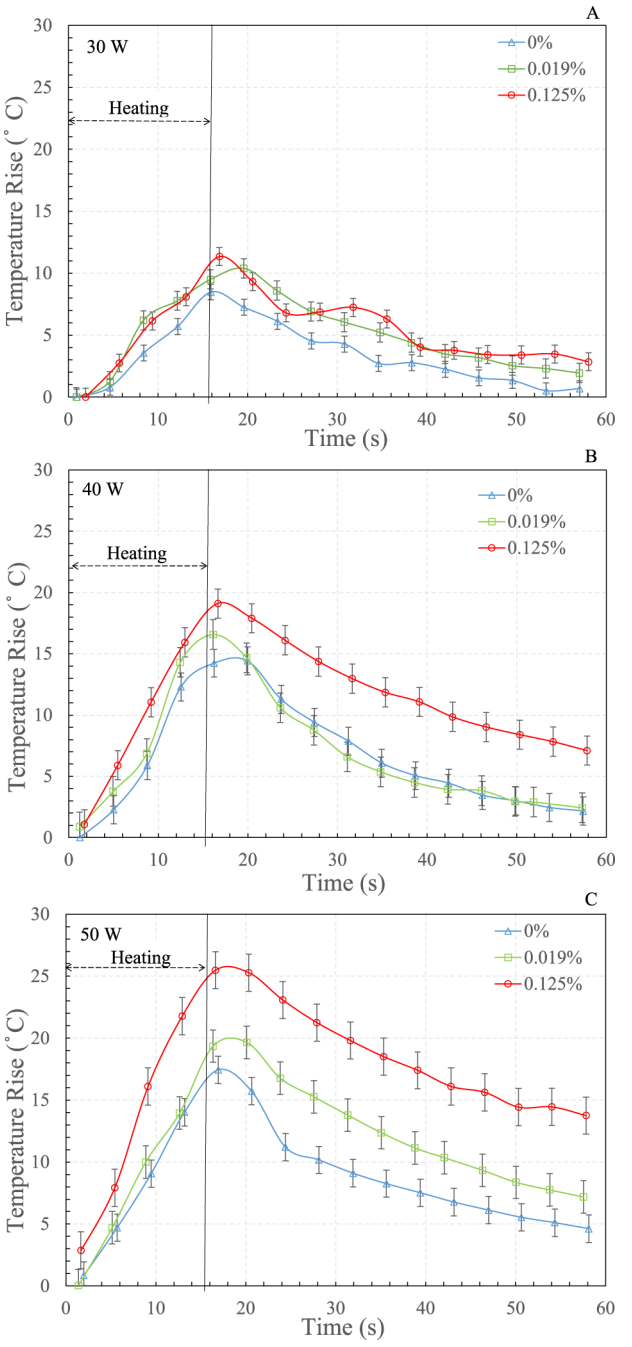

Figure 4. Comparison of the temporal variation of temperature rise (°C) using MR thermometry for the concentrations of 0%, 0.019%, and 0.125% gNPs and powers of (A) 30W, (B) 40W, and (C) 50W. The sonication period is 16s. The temporal resolution is 3s. The cooling period is 40s. The error bars represent the standard error of the values taken over the trials.

Table 2. p-values Obtained from Two-Way ANOVA Analysis

parameters	p-values
concentration	0.058
power	0.001
interaction between concentration and power	0.733

https://doi.org/10.1021/acsabm.5c00879
ACS Appl. Bio Mater. 2025, 8, 9696−9708

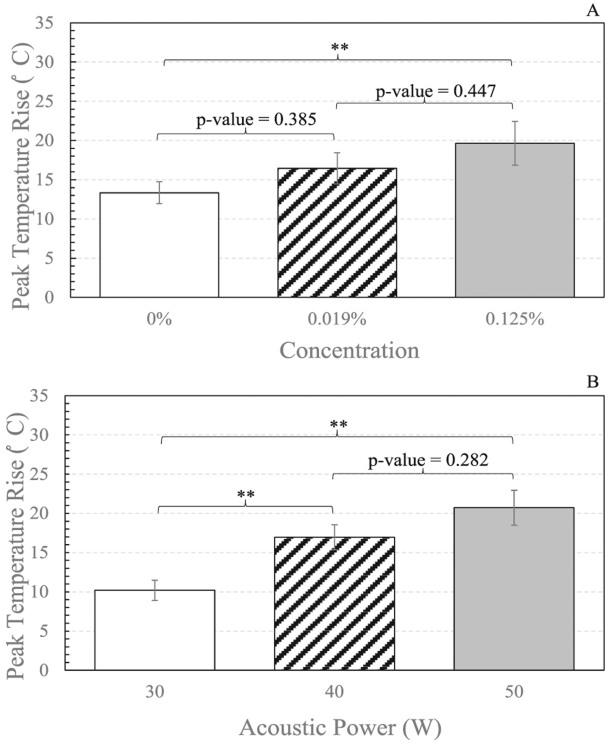

Figure 5. Group means of temperature rise for different (A) concentrations and (B) powers with *p*-values obtained by multiple comparisons of means using Tukey contrasts. (** indicates *p*-value <0.05.)

Thermal Dose. The thermal dose at the focus is computed using eq 3. Computed thermal dose values are plotted on a logarithmic scale. Figure 6 shows the thermal doses at the

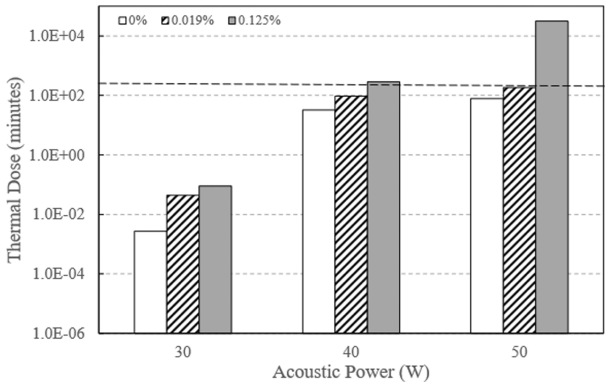

Figure 6. Thermal dose at the focus for 30W, 40W, and 50W acoustic powers and 0%, 0.019%, and 0.125% concentrations of gNPs (*Y*-axis is in log scale). The dashed horizontal line represents 240 equiv minutes.

focus for 0%, 0.019%, and 0.125% gNPs concentrations and for 30, 40, and 50W acoustic powers. The thermal dose is calculated for the average temperature rise for a series of different time points (time step = 0.5 s) over the sonication period. For the 30W power level, the thermal dose value is 2.7 $\times$ 10^{-3} min, 4.3 $\times$ 10^{-2} min, and 8.9 $\times$ 10^{-2} min for gNPs concentration of 0%, 0.019%, and 0.125%, respectively. For the 40W power level, the thermal dose values are 32.2, 93.2, and 282.9 min for gNPs concentrations of 0%, 0.019%, and 0.125%, respectively. Similarly, for the 50W power level, the thermal dose value is 77.7 min, 184.2 min, and 3.1 $\times$ 10^{4} min for gNPs concentration of 0%, 0.019%, and 0.125%, respectively. The thermal dose at the beam focus increased with both increasing acoustic power and gNPs concentration.

Number of Heating Sessions. Table 3 shows the number of heating sessions following the current protocol for 0%, 0.019%, and 0.125% gNPs concentrations and 40W and 50W acoustic powers. For the 30W power level, the number of heating sessions was >1000 for each concentration. These numbers are beyond clinical relevance. Therefore, the number of heating sessions for 30W is not included here. For the 40W power level, the number of heating sessions are 7.4, 2.6, and 0.8 for gNPs concentrations of 0%, 0.019%, and 0.125%, respectively. The number of heating sessions of 7.4 means it would require 7 full sessions and 1 shortened session, where the heating duration will be lower (0.4 times) to reach the thermal dose threshold. A similar analysis can be made for all other values in decimals. Further, the number of heating sessions is rounded up to the nearest whole number. For the 50W power level, the number of heating sessions are 3.1, 1.3, and 0.01 for gNPs concentration of 0%, 0.019%, and 0.125%, respectively. It is observed that with the increase in both the acoustic power and gNPs concentration, the number of sessions required to reach the threshold of thermal dose decreases.

Table 3. Number of Heating Sessions Required to Reach a Thermal Dose Threshold of 240 min at Different Concentrations and Powers

	number of heating sessions	
concentration	40W	50W
0%	7.4 (~8)	3.1 (~4)
0.019%	2.6 (~3)	1.3 (~2)
0.125%	0.8 (~1)	0.01 (~1)

Absorbed Energy. The amount of absorbed ultrasound energy for the 0.019% gNPs and 0.125% gNPs derived from the initial slope of the temperature trace method is provided in Table 4. The temperature rise for the initial two time-points during the sonication is used for calculating the initial slope of temperature rise with time. The absorbed energy values in Table 4 are normalized by the absorbed energy for the baseline concentration (0% gNPs) at the same power levels. For the 30W power level, approximately 1.57 times and 3.41 times the energy was absorbed for 0.019% and 0.125% concentration, respectively, compared to the baseline case. For the 40W power level, approximately 1.23 times and 2.09 times the energy was absorbed for 0.019% and 0.125% concentration, respectively, compared to the baseline case. Following a similar trend, for the 50W power level, approximately 0.82 times and 1.28 times the energy is absorbed for 0.019% and 0.125% concentration, respectively, compared to the baseline case. It is observed that the variability of absorbed energies, the measure

Table 4. Ratio of the Initial Slope of the Temperature Trace, Normalized by the Slope for the Case of 0% gNPs at Each Selected Power

	30W	40W	50W
0.019% gNPs	1.57	1.23	1.21
0.125% gNPs	3.41	2.09	1.28

https://doi.org/10.1021/acsabm.5c00879
ACS Appl. Bio Mater. 2025, 8, 9696−9708

of ratios of the initial slope, decreases (merges and approaches a value of ∼1) as the power increases.

Histopathology Using H&E Staining and IHC. Figure 7A shows the images obtained from light microscopy

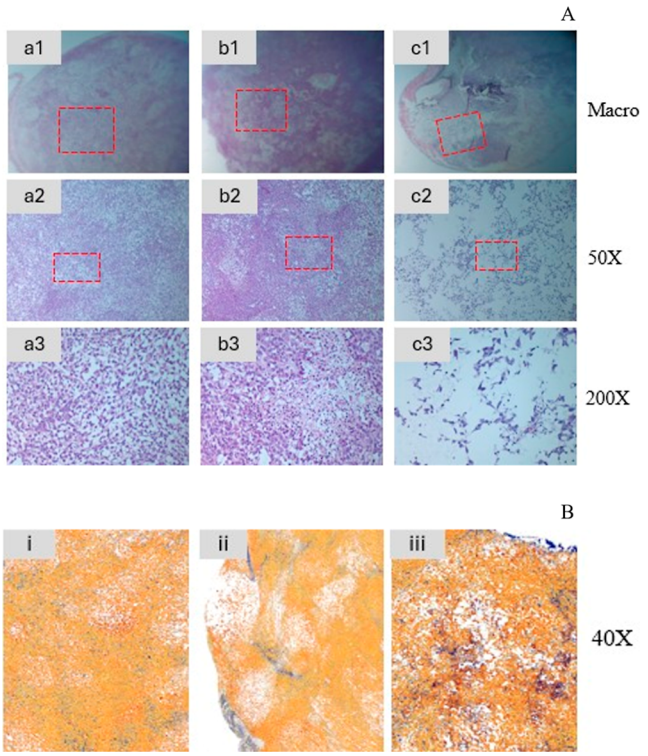

Figure 7. (A) Representative histopathology images of tumor cells near the focal zone using H&E staining. First, second, and third columns represent the mouse not receiving both gNPs and energy (column a), the mouse not receiving gNPs but receiving energy (column b), and the mouse receiving both gNPs and energy (column c), respectively. First, second, and third row (a1−a3, b1−b3, and c1−c3) represent H&E stain sections at different magnifications (Macro, 50×, and 200×, respectively). (B) Representative histopathology images of tumor cells near the focal zone using CC3 antibody staining. Images i, ii, and iii represent the mouse not receiving both gNPs and energy, the mouse not receiving gNPs but receiving energy, and the mouse receiving both gNPs and energy, respectively.

examination of H&E stain sections. The first column represents control tumor tissues receiving neither gNPs nor energy (column a). The second column represents tumors not receiving gNPs but receiving energy (column b). The third column represents tumors receiving both gNPs and energy (column c). Also, the first (a1, b1, and c1), second (a2, b2, and c2), and third (a3, b3, and c3) rows represent H&E stain sections at different magnifications (macro, 50×, and 200×, respectively). Regions of widely splayed-apart tumor cells associated with particulate debris from apparent nuclear fragmentation were more readily identified in tumors receiving both gNPs and energy (c1, c2, and c3) compared to tumors receiving neither gNPs nor energy (a1, a2, and a3) and tumors not receiving gNPs and receiving energy (b1, b2, and b3). Nuclear fragmentation leading to void formation may be associated with high energy deposition leading to cavitation and vaporization.[9]

Figure 7B shows the images obtained from examination of CC3 immunohistochemically stain sections. Images i, ii, and iii represent the mouse receiving neither gNPs nor energy, the mouse not receiving gNPs but receiving energy, and the mouse receiving both gNPs and energy, respectively. Morphometric examination of scanned, immunohistochemically stained slides using positive pixel count software (Leica) to detect CC3, a protein product arising in large amounts during the execution phase of apoptosis, observed deeply stained cells prevalent in areas of HIFU-treated tumors (brown-colored cells, panels (ii) and (iii)). It is evident that panel (iii) has relatively more brown-colored cells compared to panel (ii).

Table 5 presents the quantification of apoptotic cells based on the ratio (Nsr) of strongly positive cells (Nsp) to the total

Table 5. Quantification of Apoptotic Cells Using the Ratio of Strongly Positive Cells to Total Positive Cells

0W, 0%	50W, 0%	50W, 0.125%
0.06	0.10 (67% increase)	0.58 (10 times increase)

number of positive cells. In the control section, which received neither acoustic power nor gNPs administration, the Nsr value is the lowest at 0.06. An increase to 0.10 (67% increase) is observed for the section with an applied acoustic power of 50W and a gNPs concentration of 0%. Notably, the application of 50W acoustic power combined with 0.125% gNPs concentration results in a significantly elevated Nsr value of 0.58 (10 times increase). These findings highlight the substantial enhancement in thermal ablation efficacy achieved using gNPs.

DISCUSSION

In this section, thermal results including peak temperature rise, thermal dose, and number of heating sessions are discussed in relation to other reported studies. Then, the thermal results are compared between nonfunctionalized gNPs[10] and the Fab-functionalized gNPs assessed in the current study. Biodistribution using TEM imaging in the context of different biological mechanisms that may affect the transport of Fab-functionalized gNPs is further explained. Further, the size effect of gNPs is discussed. Additionally, histopathological results are explained. Finally, limitations of the current study and potential future work are discussed.

Thermal Results. The temperature rise was consistently higher for both 0.019% and 0.125% gNPs concentrations compared with the baseline (0% gNPs) at any power level. The temperature rise at the end of sonication for 0.019% gNPs concentration was 1.16−1.33 times higher than in the baseline case. The temperature rise at the end of sonication for 0.125% gNPs concentration was 1.33−1.65 times higher than in the baseline case. These results indicate that a higher gNPs concentration enhanced heat deposition and temperature rise. Additionally, the thermal dose at the beam focus was observed to increase when increasing both acoustic power and gNPs concentration. In the current study, two combinations (40W with 0.125% and 50W with 0.125%) were observed to reach the thermal dose threshold of 240 equiv minutes. As the goal of in vivo HIFU experiments is to reduce the collateral damage by minimizing the power requirements, the combination of 40W acoustic power and 0.125% gNPs concentration can be utilized to obtain the required thermal dose (Figure 6).

The number of heating sessions for 30W cases is observed to be higher than 1000 for each concentration, which is beyond clinical relevance. This is because the thermal dose in those

https://doi.org/10.1021/acsabm.5c00879
ACS Appl. Bio Mater. 2025, 8, 9696−9708

cases is inherently low. A potential reason for this could be the use of an acoustic gel during the experiment. During the HIFU experiment, acoustic gel (at room temperature ~25 °C) is placed between the mouse and gel pad where the mouse is positioned for HIFU treatment. This gel is provided to avoid any air gaps and bubbles in the pathway of the HIFU beam. Any bubbles or gaps can lead to cavitation. Therefore, the use of acoustic gel is a necessity. This acoustic gel in contact with the tumor lowers the body temperature of the mouse around the tumor to about 26−30 °C. HIFU heating with such a lower initial temperature may lead to a lower temperature increase, resulting in a lower thermal dose. This phenomenon has the potential to underestimate the thermal dose. This is a limitation of the study.

Previously, Devarakonda et al.[10] performed similar but not the same experiments using nonfunctionalized gNPs. The comparison between nonfunctionalized gNPs (Devarakonda et al.[10]) and Fab-functionalized gNPs (current study) have limitations because of several factors such as duration of gNPs administration, types of gNPs and its biodistribution, sonication protocol, and breed of mice. This poses challenges for a direct comparison between nonfunctionalized and Fab-functionalized gNPs at the same acoustic power of 30W and a gNPs concentration of 0.125%. Therefore, a comparison for this case has been provided as Supporting Information III. This may provide some initial insights into the contrast of utilizing functionalized and nonfunctionalized gNPs during HIFU ablation. Future studies need to be performed adopting the same methodology and duration of gNPs administration for a fair comparison.

Aggregation, Opsonization, and Clearance. TEM characterization of tumor tissue following HIFU ablation revealed the presence of Fab-functionalized gNPs in three distinct locations: within the interstitial space (arrow #1), on the surfaces of cells (arrow #2), and inside the cells (arrow #3), as shown in Figure 8. The gNPs outside the cells did not show significant aggregation. In particular, the gNPs on the surface of the cells formed linear trails of individual gNPs (arrows #2) as opposed to the gNPs inside the cells (arrows #3) that formed larger spherical aggregates. This seems to indicate the gNPs were not aggregated outside the cells but rather underwent receptor-mediated endocytosis due to the presence of Fab fragments on their surface. They were then engulfed in groups of endosomal and lysosomal vesicles. The active transport of NPs into cells using receptor-mediated endocytosis is a well-reported phenomenon that requires particles to interact with cell surface receptors prior to internalization. This appears to agree with current observations of particles lining the cell surface.[49] The absence of large aggregates in the extracellular space further implies that gNPs predominantly circulate as individual particles in the bloodstream, which may reduce the level of opsonization and delay clearance by the mononuclear phagocyte system. However, another aspect to consider is the protein corona that forms around individual gNPs in the blood: this protein corona increases the overall size of gNPs and could lead to some opsonization and thus eventual clearance.[50] Despite the potential for biomolecule adsorption to the surface of gNPs disrupting delivery, observation of gNPs in the tumor tissue suggests the effect of protein corona formation did not fully dominate the particle's fate during transport.

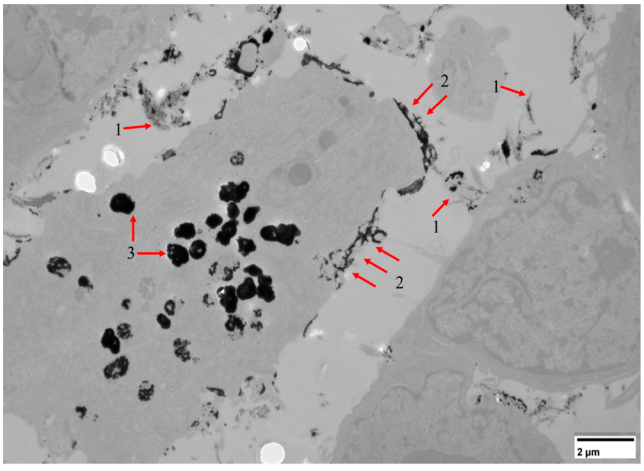

Figure 8. Aggregation, opsonization, and clearance of gNPs at within the interstitial space (arrows #1), on the surfaces of cells (arrows #2) and inside the cells (arrows #3) observed under TEM imaging.

Biophysical Mechanisms. An additional explanation for the discrepancy between the current and prior results at 30W may be due to biophysical mechanisms that affect Fab-receptor binding. The Fab used in this study contains a mutated cysteine residue for site-specific tethering to the DBCO linker via a maleimide−thiol conjugation. The site of conjugation between Fab and DBCO linker was chosen due to the ease of conjugation while also not affecting antigen binding efficiency, with no observation of overconjugation or aggregation during linker synthesis.[51] This DBCO-modified Fab linker is flexible in design such that once covalently immobilized on gNPs, the Fab construct is free to orient randomly. Randomized Fab orientation due to the linker's flexibility is expected to lead to some percentage of Fabs experiencing inhibited receptor binding due to inward-facing Fab orientations.[52] Besides the potential for random Fab orientation decreasing receptor binding, the formation of a protein corona may also inhibit Fab targeting due to biomolecule adsorption on the gNP surface that shields receptor targeting.[53] Finally, partial aggregation of Fab-coated gNPs in biological systems could also be a possibility, with the formation of larger aggregates hindering Fab binding due to either blockage of the Fab binding domains or changes in gNP size and surface area that sterically prevent Fab-receptor binding. It is important to note that the Fab-coated gNPs in this study did not exhibit aggregation in serum-mimicking solutions such as PBS. Overall, the biophysical mechanisms of distribution for gNPs that bear Fab versus untargeted gNPs indeed play a significant role in nanoparticle tumor accumulation.

Effect of the Size of gNPs. The 17 nm core diameter and 27 nm hydrodynamic diameter (core + coating) of gNPs used in this study is above the threshold gNP diameter of 10 nm that can passively enter human tissues and disrupt the normal cell environment.[54,55] The core of gNPs is known to be nontoxic and inert. The presence of gNPs without treatment is reported not to cause cellular death.[56]

Histopathology. Light microscopy examination of H&E stain sections showed an intact cellular structure for the control mice (Figure 7A, column a). Cellular debris and elongated nuclei were observed for HIFU-treated mice (Figure 7A, columns b and c). Higher numbers of deeply immunohistochemically stained cells, attributed to cellular death, were prevalent in HIFU-treated mice compared to control mice (Figure 7B). In previous reports,[10] such structures have been

https://doi.org/10.1021/acsabm.5c00879
ACS Appl. Bio Mater. 2025, 8, 9696−9708

attributed to energy-induced damage due to HIFU sonication when both H&E staining and immunohistochemistry were performed.

Limitations and Future Work. From a clinical perspective, the goal of thermal ablation is to sufficiently disrupt the tumor tissues, thereby preventing further tumor growth. Theoretically, 240 equiv minutes is regarded as a threshold thermal dose for complete tissue necrosis.[48] In the current study, two conditions exceeded this threshold: 0.125% gNPs at 40W and 0.125% gNPs at 50W. In future studies, experimental parameters, such as duration of sonication, gNPs concentration, and acoustic powers, as well as the time between injection and HIFU treatment, can be optimized to achieve the required threshold of thermal dose. It was previously[10] observed that a higher concentration of gNPs around the tumor is favorable for higher structural damage of tumor tissues. In clinical practice, functionalized gNPs could be designed to target tumors systemically by IV tail vein injection, enabling their accumulation at desired sites such as the tumor surface.[57,58] Future experiments can be conducted to assess this technique. While the present study utilized Fab-functionalized gNPs solely as thermal enhancers, several studies[59−62] have demonstrated that such NPs can also promote sustained reactive oxygen species generation and deplete intracellular glutathione, which significantly inhibits tumor progression. Future studies could explore the extent to which these mechanisms contribute to the overall therapeutic efficacy of HIFU ablation. In the current study, Fab-functionalized gNPs were characterized by using UV−vis spectroscopy, DLS, and TEM imaging. Future studies focusing on quantification and characterization as the main topic could compare NPs with different amounts of Fab conjugation on tumor uptake and HIFU efficacy. In such cases, quantification would indeed be warranted. Techniques such as UV absorbance deconvolution, SDS-PAGE, or ELISA could be employed in the future for quantification. The current study design is nonsurvival following HIFU ablation. A future survival study will allow for the assessment of tumor volume reduction. Such a survival study will require significant modification to the current protocol as well as substantial resources. The future protocol will also include simultaneous comparison of unmodified and Fab-functionalized gNPs. Further, the small sample size of the current study highlights the need for future research with a larger sample size to enhance statistical significance.

CONCLUSION

HIFU experiments with Fab-functionalized gNPs were conducted, and the results were analyzed. Successful utilization of Fab-functionalized gNPs in tumor ablation is significant because the targeting capabilities provided by these gNPs enable the HIFU ablation of deep-seated tumors such as uterine fibroids, prostate cancer, and certain brain disorders. Intratumoral administration becomes complex in deep-seated tumors. If Fab-functionalized gNPs continue to demonstrate enhanced thermal effects sufficient for tumor ablation, then their potential for IV administration allows them to be a superior therapeutic option. The presence of gNPs led to an increased temperature rise compared to baseline. Also, an increase in the concentration of gNPs resulted in an increased temperature rise. HIFU treatment at 50W power level and gNPs concentration of 0.125% showed a maximum temperature rise while producing structural tumor tissue damage. The presence of gNPs produced a higher thermal dose compared to the baseline. Additionally, the increased value of the thermal dose was observed to increase with increased concentration of gNPs. Furthermore, the number of heating sessions was reduced significantly with the use of gNPs. These findings indicate that the enhancement of local energy delivery during HIFU sonication can be achieved with the use of Fab-functionalized gNPs.

ASSOCIATED CONTENT

Supporting Information

The Supporting Information is available free of charge at https://pubs.acs.org/doi/10.1021/acsabm.5c00879.

> Synthesis and characterization of Fab-functionalized gNPs; calculation steps for the number of gNPs injection; and comparison of thermal results between nonfunctionalized and Fab-functionalized gNPs (PDF)

AUTHOR INFORMATION

Corresponding Author

Rupak K. Banerjee − *Department of Biomedical Engineering, College of Engineering and Applied Science, University of Cincinnati, Cincinnati, Ohio 45221, United States;* orcid.org/0000-0002-7235-9560; Email: banerjr@ucmail.uc.edu

Authors

Nabin Khanal − *Department of Mechanical and Materials Engineering, College of Engineering and Applied Science, University of Cincinnati, Cincinnati, Ohio 45221, United States*

Michael A. Marciniak − *Department of Chemistry and Biochemistry, University of Maryland Baltimore County (UMBC), Baltimore, Maryland 21250, United States*

Marie-Christine Daniel − *Department of Chemistry and Biochemistry, University of Maryland Baltimore County (UMBC), Baltimore, Maryland 21250, United States;* orcid.org/0000-0002-7336-5655

Liang Zhu − *Department of Mechanical Engineering, University of Maryland Baltimore County (UMBC), Baltimore, Maryland 21250, United States*

Charles Dumoulin − *Imaging Research Center (IRC), Cincinnati Children's Hospital Medical Center, Cincinnati, Ohio 45229, United States*

Keith Stringer − *Division of Pathology and Laboratory Medicine, Cincinnati Children's Hospital Medical Center, University of Cincinnati College of Medicine, Cincinnati, Ohio 45229, United States*

Matthew R. Myers − *Division of Solid and Fluid Mechanics, Center for Devices and Radiology Health, U.S. Food and Drug Administration, Silver Spring, Maryland 20993, United States*

Pavel Yarmolenko − *Sheikh Zayed Institute for Pediatric Surgical Innovation, Children's National Hospital, Washington, District of Columbia 20012, United States*

Complete contact information is available at: https://pubs.acs.org/10.1021/acsabm.5c00879

Notes

The authors declare no competing financial interest.

https://doi.org/10.1021/acsabm.5c00879
ACS Appl. Bio Mater. 2025, 8, 9696−9708

■ ACKNOWLEDGMENTS

The authors wish to acknowledge and thank the Imaging Research Center (IRC), the Comprehensive Rodent and Radiation Facility, and the Division of Pathology and Laboratory Medicine at Cincinnati Children's Hospital Medical Center (CCHMC). In particular, we are thankful to Matthew Lanier's technical assistance with the HIFU system, Victoria Summey and Jeffrey Bailey's assistance with managing animals, and Chris Woods for technical assistance with digitally scanned slides. We are also very grateful for the HIFU data postprocessing suggestions provided to us by Ari Partanen of Profound Medical. We are also thankful to Dr. Marepalli Rao at the Department of Biostats, Health Information and Data Science, University of Cincinnati, for his assistance with statistical analysis. In addition, we are also thankful to the National Science Foundation (NSF) for supporting this research through the grant #NSF CBET 2045234.

■ REFERENCES

(1) Anik, M. I.; Mahmud, N.; Al Masud, A.; Hasan, M. Gold nanoparticles (GNPs) in biomedical and clinical applications: A review. *Nano Sel.* **2022**, *3* (4), 792.

(2) Fan, T.; Liu, Z.; Zhang, D.; Tang, M. Comparative study of lesions created by high-intensity focused ultrasound using sequential discrete and continuous scanning strategies. *IEEE Trans. Biomed. Eng.* **2013**, *60* (3), 763−769.

(3) Ahmad Reza Dibaji, S.; Al-Rjoub, M. F.; Myers, M. R.; Banerjee, R. K. Enhanced heat transfer and thermal dose using magnetic nanoparticles during HIFU thermal ablation-an in-vitro study. *J. Nanotechnol. Eng. Med.* **2013**, *4* (4), 040902.

(4) Gambin, B.; Kruglenko, E. Ultrasonic specific absorption rate in nanoparticle-mediated moderate hyperthermia. *Bull. Pol. Acad. Sci.:Tech. Sci.* **2021**, *69* (3), 137053.

(5) Wu, Y.; Xie, H.; Wang, Y.; Wang, B.; Cao, H. Study of the viscous heating effect of particle enhancers in focused ultrasound based on the theory of two-phase media. *Appl. Acoust.* **2025**, *229*, 110391.

(6) Devarakonda, S. B.; Myers, M. R.; Lanier, M.; Dumoulin, C.; Banerjee, R. K. Assessment of Gold Nanoparticle-Mediated-Enhanced Hyperthermia Using MR-Guided High-Intensity Focused Ultrasound Ablation Procedure. *Nano Lett.* **2017**, *17* (4), 2532−2538.

(7) Merckel, L. G.; Knuttel, F. M.; Deckers, R.; van Dalen, T.; Schubert, G.; Peters, N. H.; Weits, T.; van Diest, P. J.; Mali, W. P.; Vaessen, P. H.; van Gorp, J. M.; Moonen, C. T.; Bartels, L. W.; van den Bosch, M. A. First clinical experience with a dedicated MRI-guided high-intensity focused ultrasound system for breast cancer ablation. *Eur. Radiol.* **2016**, *26* (11), 4037−4046.

(8) Knuttel, F. M.; van den Bosch, M. A. Magnetic Resonance-Guided High Intensity Focused Ultrasound Ablation of Breast Cancer. *Adv. Exp. Med. Biol.* **2016**, *880*, 65−81.

(9) Fruehauf, J. H.; Back, W.; Eiermann, A.; Lang, M. C.; Pessel, M.; Marlinghaus, E.; Melchert, F.; Volz-Köster, S.; Volz, J. High-intensity focused ultrasound for the targeted destruction of uterine tissues: experiences from a pilot study using a mobile HIFU unit. *Arch. Gynecol. Obstet.* **2008**, *277* (2), 143−150.

(10) Devarakonda, S. B.; Stringer, K.; Rao, M.; Myers, M.; Banerjee, R. Assessment of Enhanced Thermal Effect Due to Gold Nanoparticles during MR-Guided High-Intensity Focused Ultrasound (HIFU) Procedures Using a Mouse-Tumor Model. *ACS Biomater. Sci. Eng.* **2019**, *5* (8), 4102−4111.

(11) Khanal, N., Marciniak, M., Daniel, M., Zhu, L., Lanier, M., Dumoulin, C., Banerjee, R. K. Functionalized nanoparticles mediated high intensity focused ultrasound (HIFU) ablation in mice. In *Proceedings of the Summer Biomechanics, Bioengineering and Biotransport Conference*: Lake Geneva, WI, USA, 11−14 June 2024; SB3C2024-531, 2024.

(12) Rosnitskiy, P. B.; Yuldashev, P. V.; Sapozhnikov, O. A.; Maxwell, A. D.; Kreider, W.; Bailey, M. R.; Khokhlova, V. A. Design of HIFU Transducers for Generating Specified Nonlinear Ultrasound Fields. *IEEE Trans. Ultrason. Ferroelectrics Freq. Control* **2017**, *64* (2), 374−390.

(13) Liu, S.; Yang, Y.; Li, C.; Guo, X.; Tu, J.; Zhang, D. Prediction of HIFU Propagation in a Dispersive Medium via Khokhlov−Zabolotskaya−Kuznetsov Model Combined with a Fractional Order Derivative. *Appl. Sci.* **2018**, *8* (4), 609.

(14) Devarakonda, S.; Ahmad Reza Dibaji, S.; Hariharan, P.; Myers, M. R.; Banerjee, R. K. Characterization of Focal Location During High-Intensity Focused Ultrasound Ablation in a Tissue Phantom Using Remote Thermocouple Arrays1. *J. Med. Dev.* **2021**, *10* (2), 020949.

(15) Mohammadi, M.; Rafii-Tabar, H. Modeling hyperthermia-based prostate cancer treatment in the presence of core-shell nanoparticles and large blood vessels under different ultrasound sonication patterns. *Int. J. Therm. Sci.* **2024**, *203*, 109123.

(16) Warmt, E.; Kießling, T. R.; Stange, R.; Fritsch, A. W.; Zink, M.; Käs, J. A. Thermal instability of cell nuclei. *New J. Phys.* **2014**, *16* (7), 073009.

(17) Zhang, N.; Cai, X.; Gao, W.; Wang, R.; Xu, C.; Yao, Y.; Hao, L.; Sheng, D.; Chen, H.; Wang, Z.; Zheng, Y. A Multifunctional Theranostic Nanoagent for Dual-Mode Image-Guided HIFU/Chemo- Synergistic Cancer Therapy. *Theranostics* **2016**, *6* (3), 404−417.

(18) Sathaworawong, A.; Wanitphakdeedecha, R. Nerve injury associated with high-intensity focused ultrasound: A case report. *J. Cosmet. Dermatol.* **2018**, *17* (2), 162−164.

(19) Romano, C. L.; Romano, D.; Logoluso, N. Low-intensity pulsed ultrasound for the treatment of bone delayed union or nonunion: a review. *Ultrasound Med. Biol.* **2009**, *35* (4), 529−536.

(20) Xue, X.; Song, Q.; Yang, X.; Kuati, A.; Fu, H.; Liu, Y.; Cui, G. Effect of extracorporeal shockwave therapy for rotator cuff tendinopathy: a systematic review and meta-analysis. *BMC Muscoskelet. Disord.* **2024**, *25* (1), 357.

(21) McLaughlan, J. R.; Cowell, D. M. J.; Freear, S. Gold nanoparticle nucleated cavitation for enhanced high intensity focused ultrasound therapy. *Phys. Med. Biol.* **2018**, *63* (1), 015004.

(22) Canavese, G.; Ancona, A.; Racca, L.; Canta, M.; Dumontel, B.; Barbaresco, F.; Limongi, T.; Cauda, V. Nanoparticle-assisted ultrasound: A special focus on sonodynamic therapy against cancer. *Chem. Eng. J.* **2018**, *340*, 155−172.

(23) Zhou, Y.; Han, X.; Jing, X.; Chen, Y. Construction of Silica-Based Micro/Nanoplatforms for Ultrasound Theranostic Biomedicine. *Adv. Healthcare Mater.* **2017**, *6* (18), 1700646.

(24) Bera, C.; Devarakonda, S. B.; Kumar, V.; Ganguli, A. K.; Banerjee, R. K. The mechanism of nanoparticle-mediated enhanced energy transfer during high-intensity focused ultrasound sonication. *Phys. Chem. Chem. Phys.* **2017**, *19* (29), 19075−19082.

(25) Liao, M.; Du, J.; Chen, L.; Huang, J.; Yang, R.; Bao, W.; Zeng, K.; Wang, W.; Aphan, B. C.; Wu, Z.; Ma, L.; Lu, Q. Sono-activated materials for enhancing focused ultrasound ablation: Design and application in biomedicine. *Acta Biomater.* **2024**, *173*, 36−50.

(26) Yang, P.; Zhi, X.; Xu, Y.; Qian, L.; Dai, Z. Nanomedicines enhance minimally invasive therapy of pancreatic cancer. *Nano Today* **2023**, *51*, 101891.

(27) Wust, P.; Gneveckow, U.; Wust, P.; Gneveckow, U.; Johannsen, M.; Böhmer, D.; Henkel, T.; Kahmann, F.; Sehouli, J.; Felix, R.; et al. Magnetic nanoparticles for interstitial thermotherapy–feasibility, tolerance and achieved temperatures. *Int. J. Hyperthermia* **2006**, *22* (8), 673−685.

(28) Beik, J.; Abed, Z.; Ghadimi-Daresajini, A.; Nourbakhsh, M.; Shakeri-Zadeh, A.; Ghasemi, M. S.; Shiran, M. B. Measurements of nanoparticle-enhanced heating from 1 MHz ultrasound in solution and in mice bearing CT26 colon tumors. *J. Therm. Biol.* **2016**, *62* (Pt A), 84−89.

(29) Devarakonda, S. B.; Myers, M. R.; Giridhar, D.; Dibaji, S. A.; Banerjee, R. K. Enhanced thermal effect using magnetic nano-particles

https://doi.org/10.1021/acsabm.5c00879
ACS Appl. Bio Mater. 2025, 8, 9696−9708

during high-intensity focused ultrasound. *PLoS One* **2017**, *12* (4), No. e0175093.
(30) Kaczmarek, K.; Hornowski, T.; Bielas, R.; Żak, D.; Timko, M.; Józefczak, A. Dependence of Ultrasonic and Magnetic Hyperthermia on the Concentration of Magnetic Nanoparticles. *Acta Phys. Polym., A* **2018**, *133* (3), 716−718.
(31) Sadeghi-Goughari, M.; Jeon, S.; Kwon, H. J. Enhancing Thermal Effect of Focused Ultrasound Therapy Using Gold Nanoparticles. *IEEE Trans. NanoBioscience* **2019**, *18* (4), 661−668.
(32) Mochalova, E. N.; Egorova, E. A.; Komarova, K. S.; Shipunova, V. O.; Khabibullina, N. F.; Nikitin, P. I.; Nikitin, M. P. Comparative Study of Nanoparticle Blood Circulation after Forced Clearance of Own Erythrocytes (Mononuclear Phagocyte System-Cytoblockade) or Administration of Cytotoxic Doxorubicin- or Clodronate-Loaded Liposomes. *Int. J. Mol. Sci.* **2023**, *24* (13), 10623.
(33) Hoshyar, N.; Gray, S.; Han, H.; Bao, G. The effect of nanoparticle size on in vivo pharmacokinetics and cellular interaction. *Nanomedicine* **2016**, *11* (6), 673−692.
(34) Luan, X.; Kong, H.; He, P.; Yang, G.; Zhu, D.; Guo, L.; Wei, G. Self-Assembled Peptide-Based Nanodrugs: Molecular Design, Synthesis, Functionalization, and Targeted Tumor Bioimaging and Biotherapy. *Small* **2023**, *19* (3), No. e2205787.
(35) Seidu, T. A.; Kutoka, P. T.; Asante, D. O.; Farooq, M. A.; Alolga, R. N.; Bo, W. Functionalization of Nanoparticulate Drug Delivery Systems and Its Influence in Cancer Therapy. *Pharmaceutics* **2022**, *14* (5), 1113.
(36) Wang, C.; Shen, Z.; Chen, Y.; Wang, Y.; Zhou, X.; Chen, X.; Li, Y.; Zhang, P.; Zhang, Q. Research Progress on Cyclic-Peptide Functionalized Nanoparticles for Tumor-Penetrating Delivery. *Int. J. Nanomedicine* **2024**, *19*, 12633−12652.
(37) Ouyang, B.; Poon, W.; Zhang, Y. N.; Lin, Z. P.; Kingston, B. R.; Tavares, A. J.; Zhang, Y.; Chen, J.; Valic, M. S.; Syed, A. M.; MacMillan, P.; Couture-Senécal, J.; Zheng, G.; Chan, W. C. W. The dose threshold for nanoparticle tumour delivery. *Nat. Mater.* **2020**, *19* (12), 1362−1371.
(38) Khanal, N., Summey, V., Bailey, J., Duan, X., Zhu, L., Banerjee, R. K. Developing Mouse-Tumor Model for High Intensity Focused Ultrasound (HIFU) Ablation Procedures. In *Proceedings of the Summer Biomechanics, Bioengineering and Biotransport Conference*: Lake Geneva, WI, USA, 11−14 June 2024; SB3C2024-512, 2024.
(39) Khanal, N.; Summey, V.; Bailey, J.; Duan, X.; Zheng, Y.; Zhu, L.; Stringer, K.; Rao, M.; Banerjee, R. K. Development of Mouse-Tumor Model Using Prostate Cancer (PC3) Cell Line for High-Intensity Focused Ultrasound (HIFU) Ablation. *Prostate Cancer* **2025**, *2025*, 5678314.
(40) Coughlan, A. M.; Harmon, C.; Whelan, S.; O'Brien, E. C.; O'Reilly, V. P.; Crotty, P.; Kelly, P.; Ryan, M.; Hickey, F. B.; O'Farrelly, C.; Little, M. A. Myeloid Engraftment in Humanized Mice: Impact of Granulocyte-Colony Stimulating Factor Treatment and Transgenic Mouse Strain. *Stem Cells Dev.* **2016**, *25* (7), 530−541.
(41) Shultz, L. D.; Lyons, B. L.; Burzenski, L. M.; Gott, B.; Chen, X.; Chaleff, S.; Kotb, M.; Gillies, S. D.; King, M.; Mangada, J.; Greiner, D. L.; Handgretinger, R. Human lymphoid and myeloid cell development in NOD/LtSz-scid IL2R gamma null mice engrafted with mobilized human hemopoietic stem cells. *J. Immunol.* **2005**, *174* (10), 6477−6489.
(42) Dockery, L. T.; Daniel, M. C. Targeted Doxorubicin-Loaded Dendronized Gold Nanoparticles. *Pharmaceutics* **2023**, *15* (8), 2103.
(43) Dockery, L.; Zalesak-Kravec, S.; Kane, M. A.; Daniel, M. C. Modular and efficient synthesis of a poly (propylene imine) (PPI) dendron applied to acid-sensitive doxorubicin conjugation. *Tetrahedron* **2022**, *125*, 133044.
(44) Gu, Q.; Zhu, L. Heating Induced Nanoparticle Migration and Enhanced Delivery in Tumor Treatment Using Nanotechnology. *Bioeng.* **2024**, *11* (9), 900.
(45) Gu, Q.; Dockery, L.; Daniel, M. C.; Bieberich, C. J.; Ma, R.; Zhu, L. Nanoparticle Delivery in Prostate Tumors Implanted in Mice Facilitated by Either Local or Whole-Body Heating. *Fluids* **2021**, *6* (8), 272.
(46) Li, X.; Wang, B.; Zhou, S.; Chen, W.; Chen, H.; Liang, S.; Zheng, L.; Yu, H.; Chu, R.; Wang, M.; Chai, Z.; Feng, W. Surface chemistry governs the sub-organ transfer, clearance and toxicity of functional gold nanoparticles in the liver and kidney. *J. Nanobiotechnol.* **2020**, *18* (1), 45.
(47) Yu, M.; Zheng, J. Clearance Pathways and Tumor Targeting of Imaging Nanoparticles. *ACS Nano* **2015**, *9* (7), 6655−6674.
(48) Sapareto, S. A.; Dewey, W. C. Thermal dose determination in cancer therapy. *Int. J. Radiat. Oncol., Biol., Phys.* **1984**, *10* (6), 787−800.
(49) Li, R.; Zheng, K.; Yuan, C.; Chen, Z.; Huang, M. Be Active or Not: the Relative Contribution of Active and Passive Tumor Targeting of Nanomaterials. *Nanotheranostics* **2017**, *1* (4), 346−357.
(50) Zanganeh, S.; Spitler, R.; Erfanzadeh, M.; Alkilany, A. M.; Mahmoudi, M. Protein corona: Opportunities and challenges. *Int. J. Biochem. Cell Biol.* **2016**, *75*, 143−147.
(51) Florinas, S.; Liu, M.; Fleming, R.; Van Vlerken-Ysla, L.; Ayriss, J.; Gilbreth, R.; Dimasi, N.; Gao, C.; Wu, H.; Xu, Z. Q.; Chen, S.; Dirisala, A.; Kataoka, K.; Cabral, H.; Christie, R. J. A Nanoparticle Platform To Evaluate Bioconjugation and Receptor-Mediated Cell Uptake Using Cross-Linked Polyion Complex Micelles Bearing Antibody Fragments. *Biomacromolecules* **2016**, *17* (5), 1818−1833.
(52) Saha, B.; Songe, P.; Evers, T. H.; Prins, M. W. J. The influence of covalent immobilization conditions on antibody accessibility on nanoparticles. *Analyst* **2017**, *142* (22), 4247−4256.
(53) Kim, W.; Ly, N. K.; He, Y.; Li, Y.; Yuan, Z.; Yeo, Y. Protein corona: Friend or foe? Co-opting serum proteins for nanoparticle delivery. *Adv. Drug Delivery Rev.* **2023**, *192*, 114635.
(54) Nguyen, L. N. M.; Lin, Z. P.; Sindhwani, S.; MacMillan, P.; Mladjenovic, S. M.; Stordy, B.; Ngo, W.; Chan, W. C. W. The exit of nanoparticles from solid tumours. *Nat. Mater.* **2023**, *22* (10), 1261−1272.
(55) Vishwakarma, V.; Samal, S. S.; Manoharan, N. Safety and Risk Associated with Nanoparticles - A Review. *J. Miner. Mater. Charact. Eng.* **2010**, *09* (05), 455−459.
(56) Murphy, C. J.; Gole, A. M.; Stone, J. W.; Sisco, P. N.; Alkilany, A. M.; Goldsmith, E. C.; Baxter, S. C. Gold nanoparticles in biology: beyond toxicity to cellular imaging. *Acc. Chem. Res.* **2008**, *41* (12), 1721−1730.
(57) Al-Jamal, W. T.; Al-Jamal, K. T.; Tian, B.; Cakebread, A.; Halket, J. M.; Kostarelos, K. Tumor targeting of functionalized quantum dot-liposome hybrids by intravenous administration. *Mol. Pharmaceutics* **2009**, *6* (2), 520−530.
(58) Cheng, J.; Teply, B. A.; Sherifi, I.; Sung, J.; Luther, G.; Gu, F. X.; Levy-Nissenbaum, E.; Radovic-Moreno, A. F.; Langer, R.; Farokhzad, O. C. Formulation of functionalized PLGA-PEG nanoparticles for in vivo targeted drug delivery. *Biomaterials* **2007**, *28* (5), 869−876.
(59) Chiang, M. R.; Hsu, C. W.; Pan, W. C.; Tran, N. T.; Lee, Y. S.; Chiang, W. H.; Liu, Y. C.; Chen, Y. W.; Chiou, S. H.; Hu, S. H. Reprogramming Dysfunctional Dendritic Cells by a Versatile Catalytic Dual Oxide Antigen-Captured Nanosponge for Remotely Enhancing Lung Metastasis Immunotherapy. *ACS Nano* **2025**, *19* (2), 2117−2135.
(60) Yalamandala, B. N.; Chen, Y. J.; Lin, Y. H.; Huynh, T. M. H.; Chiang, W. H.; Chou, T. C.; Liu, H. W.; Huang, C. C.; Lu, Y. J.; Chiang, C. S.; Chu, L. A.; Hu, S. H. A Self-Cascade Penetrating Brain Tumor Immunotherapy Mediated by Near-Infrared II Cell Membrane-Disrupting Nanoflakes via Detained Dendritic Cells. *ACS Nano* **2024**, *18* (28), 18712−18728.
(61) Huynh, T. M. H.; Luc, V.-S.; Chiang, M.-R.; Weng, W.-H.; Chang, C.-W.; Chiang, W.-H.; Liu, Y.-C.; Chuang, C.-Y.; Chang, C.-C.; Hu, S.-H. Programmed Lung Metastasis Immunotherapy via Cascade-Responsive Cell Membrane-Mimetic Copolymer-Wrapped Nanoraspberry-Mediated Elesclomol-Copper Delivery. *Adv. Funct. Mater.* **2024**, *34* (34), 2401806.
(62) Yalamandala, B. N.; Moorthy, T.; Liu, Z. H.; Huynh, T. M. H.; Iao, H. M.; Pan, W. C.; Wang, K. L.; Chiang, C. S.; Chiang, W. H.; Liao, L. D.; Liu, Y. C.; Hu, S. H. A Self-Cascading Catalytic Therapy

https://doi.org/10.1021/acsabm.5c00879
ACS Appl. Bio Mater. 2025, 8, 9696−9708

and Antigen Capture Scaffold-Mediated T Cells Augments for Postoperative Brain Immunotherapy. *Small* **2025**, *21* (5), No. e2406178.

https://doi.org/10.1021/acsabm.5c00879
ACS Appl. Bio Mater. 2025, 8, 9696−9708